

2- μm high-power multiple-frequency single-mode Q-switched Ho:YLF laser for DIAL application

Fabien Gibert · Dimitri Edouart · Claire Cénac · Florian Le Mounier

Received: 24 September 2013 / Accepted: 28 January 2014 / Published online: 13 February 2014
© The Author(s) 2014. This article is published with open access at Springerlink.com

Abstract We report on the development and the demonstration of a two-wavelength single-frequency laser oscillator based on Ho:YLF crystal. This laser is especially suitable for application as a transmitter in differential absorption lidar (DIAL)/integrated path differential absorption (IPDA) measurements of atmospheric carbon dioxide (CO_2) using the R30 CO_2 absorption line at 2,050.967 nm. The oscillator consists in a fiber-coupled and free-space solid-state hybrid system and can be used in high-energy middle-rate or moderate-energy high-rate configurations. The latter produced On and Off sequentially single-frequency laser pulses with 13 mJ of energy at a repetition rate of 2 kHz and pulse duration of 42 ns. The pulse energy and frequency stabilities are specially documented in free-running, single-frequency and two-frequency seeding single-mode operations. Standard deviation is 7.7 % for pulse energy and 2 MHz for frequency stability for the two-wavelength seeding operation. Allan variance plot shows that frequency fluctuations are reduced below 70 kHz for 10 s of averaging which is suitable for accurate CO_2 DIAL or IPDA measurements.

1 Introduction

2- μm solid-state lasers have applications in several domains including remote sensing, medicine, material processing and defense. Concerning remote sensing, these lasers benefit from an emission in the eye-safe domain to be used as lidar emitter in a differential absorption lidar

(DIAL) configuration for remote trace gas monitoring (mainly H_2O and CO_2) or in a coherent lidar for wind detection [1–4]. In the context of greenhouse gases monitoring such as carbon dioxide (CO_2), a powerful emitter in the near infrared (1.5–2 μm) is needed to get a useful precision on concentration measurement (<1 %) with reasonably space and time resolution at a distance of several kilometers. Energy pulses larger than several millijoules at a pulse repetition frequency (PRF) larger than several hundred of Hertz are usually required. Such requirements call for a solid-state laser configuration at least for a part of it as demanded pulse energy is well beyond current pulsed fiber laser potential performances. These DIAL emitters also call for a specific multiple wavelength emission around the chosen atmospheric gas absorption line, single-mode operation, high spectral purity and stability, high pulse energy stability, good beam quality, linear pulse polarization and good overall wall plug efficiency, especially for space integrated path differential absorption (IPDA) lidar measurements. Furthermore, high pulse energy (>20 mJ) at moderate PRF (100 Hz) (HE–MR) or moderate pulse energy (<1 mJ) at high PRF (10 kHz) (ME–HR) concepts are both needed (depending on the detection of the DIAL system, i.e., direct or heterodyne) for applications such as global monitoring from space [5, 6], ground-based 3-D monitoring above anthropogenic emissive sites [7–9] (cities, plants, carbon capture and storage sites, volcano area) and eddy covariance flux calculations [10].

Traditionally, high-energy single-mode Q-switched operation in the 2- μm region is achieved with side-pumped Tm,Ho:YLF or Tm,Ho:LuLF lasers [1–4]. However, the efficiency of these systems is usually limited because of the deleterious effect of upconversion losses at high pump level and reverse transfer between the Tm and Ho ions [11]

F. Gibert (✉) · D. Edouart · C. Cénac · F. Le Mounier
Laboratoire de Météorologie Dynamique, Institut Pierre et
Simon Laplace, Ecole Polytechnique, Palaiseau, France
e-mail: fabien.gibert@lmd.polytechnique.fr

which produce a large thermal load of the crystal and practically prevent an operation at PRF larger than few tens of Hertz. Further work has then focussed on direct in-band pumping of the Ho 5I_7 manifold by Tm:YLF solid-state laser [12, 13] or more recently by suitable laser diodes at 1.9 μm [14] or via a diode-pumped secondary laser source, e.g., a thulium (Tm) fiber laser [15]. Even if the Tm-fiber lasers are diode-pumped in the 790 nm band leading to an a priori large quantum defect, the electrical to optical efficiency (EOE) can be significantly enhanced by the cross-relaxation process where one photon can excite two Tm ions in the 3H_4 level [11, 16]. Current commercial Tm fiber laser from the supplier ITF Labs (15 W module), reaches an EOE of 20 %, similar to current 1.9 μm laser diode module efficiency [17] but with outstanding properties concerning the beam quality, the narrow linewidth (<0.5 nm) and robustness.

A precursor work of Bollig et al. [18, 19] demonstrated an injection-seeded single-frequency Q-switched Ho:YLF master oscillator power amplifier (MOPA) pumped by a Tm fiber laser which delivers 70 mJ per pulse at 50 Hz repetition rate at 2,064 nm. Seeding was performed using an internal-modulated distributed-feedback laser diode (DFB) with a Pound-Drever-Hall (PDH) technique to lock the oscillator cavity length [20]. However, the fully characterization of the Q-switched seeded operation in terms of pulse energy and frequency stability and purity which is fundamental for a DIAL emitter has not yet been reported. In addition, a DIAL emitter requires at least a two-wavelength single-mode operation with the same oscillator which entails an additional challenge for HE-MR and ME-HR Ho:YLF oscillators.

In this paper, we present the achievement of a two-wavelength injection-seeded single-mode Q-switched fiber laser pumped Ho:YLF oscillator. The specific application of this laser, i.e., DIAL measurements of atmospheric CO_2 , requires an emission in the 2,050-nm band around the specific R30 CO_2 absorption line at 2,050.967 nm [21, 22]. First, we describe the experimental set-up of the pulsed oscillator especially the injection-seeding scheme. Secondly, the results in free-running, single-frequency and two-frequency injection-seeding operations are reported. These results are discussed in the framework of DIAL requirements for ground-based, airborne or space application.

2 Experimental set-up

Numerical simulations have been performed using a two-dimensional rotational symmetric Gaussian rate equations model (inspired by the work of Barnes et al. [23]) to design the pumping scheme and the Ho:YLF crystal characteristics

(Ho doping, crystal length, emission wavelength and output coupler transmission, maximum intra-cavity fluence). Complementary Zemax software simulations brought the characteristics of the resonator (cavity length, mirror characteristics). The main objective was to design an optimized compact ME-HR DIAL emitter (PRF > 1 kHz) to be associated with a coherent detection in order to reach the requirements on CO_2 mixing ratio measurements in Gibert et al. [10]. The DIAL emitter may also work in a HE-MR concept (although not fully optimized in this paper) in order to be associated with a direct detection for further airborne or space application once efficient avalanche photodiodes will be available in the 2- μm domain. The oscillator is a hybrid system which benefits from both new fiber-coupled devices at 2 μm for compactness [Tm fiber laser pump, seeding module, frequency reference system (FRS)] and free-space solid-state laser to get high pulse energy operation. The free-space cavity stands on a 300×300 mm² optical bench. The experimental set-up is displayed in Fig. 1.

2.1 Ho:YLF ring laser

A 100-W linearly polarized Tm-fiber laser (model TLR-100-1940-LP from IPG Photonics) is used to end pump a 80-mm long 0.5 %-doped Ho:YLF crystal rod on the π -polarization. The Tm-fiber laser delivered a 5-mm-diameter collimated beam. The pump beam size is reduced to approximately 1 mm diameter along the Ho:YLF crystal rod using a telescope with two lenses of 150 and -30 mm focal lengths. The distance between the two lenses can be adjusted to fine tune the pump beam size to the resonator mode size in the Ho:YLF crystal and to compensate for thermal lensing. A dry-air circulation was set up along the laser pump beam propagation to avoid water vapor absorption. The Ho:YLF crystal end faces are tilted by approximately 3° and antireflection coated for 1,940 and 2,050 nm. A water-cooled copper mount enables the setting of the crystal rod temperature at 15 $^\circ\text{C}$ which was chosen as compromise to get the maximum gain of the crystal and avoid water vapor condensation on the crystal free faces.

The Ho:YLF crystal is positioned inside a ring resonator built with two flat dichroic mirrors (HT @ 1,940 nm and HR @ 2,050 nm), a 1-m concave high reflector mounted on a piezo-transducer (PZT from Cedrat Technologies, HPPA-8) and a 50 % reflective 1-m concave output coupler. A reflectivity larger than 50 % of the output coupler is necessary to reach the specific Ho:YLF emission band around 2,051 nm of interest and R30 CO_2 absorption line. The 2,051 nm emission band is indeed in competition with a second emission band around 2,065 nm that is usually emitted with lower-transmission output coupler [15]. We

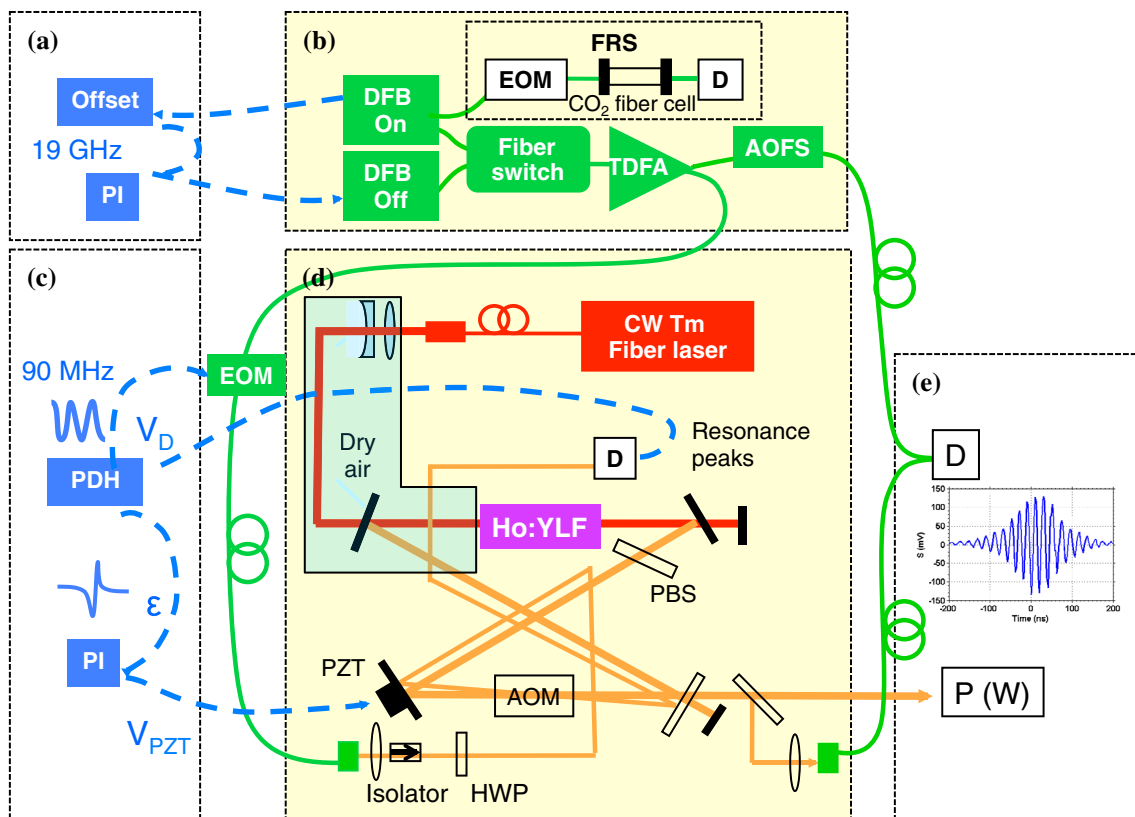


Fig. 1 Experimental set-up. **a** Offset locking between On and Off distributed-feedback laser diode (DFB), **b** seeding architecture, **c** cavity length locking using Pound-Drever-Hall technique (PDH), **d** 2- μm pulsed oscillator. **e** Characterization: power meter, beam profiler, heterodyne detection. *FRS* frequency reference system;

TDFA thulium-doped fiber amplifier; *D* detector; *AOM* acousto-optic modulator; *AOFS* acousto-optic frequency shifter (50 MHz); *EOM* electro-optic modulator; *PI* proportional integral servo-controller; *PZT* piezoelectric actuator; *HWP* half-wave plate; *PBS* polarizer beam splitter. Optical couplers are not displayed

use a 1-m long ring cavity (1) to get short pulse duration (<100 ns) and consequently to increase the number of independent samples for a coherent DIAL system [24], (2) to ease injection-seeding operation and avoid spatial hole burning effect (the unidirectional operation is enforced using a 1-m concave high reflector after the output coupler) and (3) to keep a reasonable intra-cavity space to include all optical elements. Neglecting thermal lensing, the calculated TEM_{00} beam radius in the crystal was around $410 \mu\text{m}$. This was supposed to increase at higher pump power due to the negative thermal lensing effect in Ho:YLF crystal. An acousto-optic modulator (AOM) from Gooch and Housego (QS027-10 M-NL5) positioned at Bragg angle is used for Q-switch operation. Thus, the PRF can be adjusted to address both HE-MR and ME-HR concepts for a DIAL emitter associated with direct and heterodyne detection, respectively. A 27-MHz radiofrequency wave at 100 W peak power achieves an 80 % diffraction efficiency of the AOM. In addition to the effect of the natural birefringent properties of YLF crystal, a polarizer beam splitter (PBS) was inserted inside the cavity to ensure a linear π -polarization of the master oscillator.

The crystal orientation was finely adjusted to avoid Lyot filtering effect in the laser gain bandwidth.

2.2 Injection-seeding scheme

Two distributed-feedback laser diode (DFB) from Nanoplus GmbH are used to seed the 2- μm pulsed oscillator. Both DFBs are fiber-coupled and deliver up to 4 mW in the fiber with a narrow linewidth of approximately 2 MHz (FWHM). A built-in 30 dB isolator prevents feedback from the following fiber-coupled components. An optical fiber switch from Photlines Technologies (SWT-LN-2000-2X2) enables to sequentially seed the pulsed oscillator with the two wavelengths at a repetition rate up to tens of kHz. Cross-talk isolation of the switch is around 20 dB, and switching time is 100 ns [25]. A thulium-doped fiber amplifier (TDFA) designed at Office National d'Etude et de Recherche Aérospatiale (ONERA) is used to compensate for all the insertion losses introduced by each fiber-coupled component and provide enough power for both seeding and coherent detection. All fiber-coupled components are polarization maintaining (PM) to avoid laser

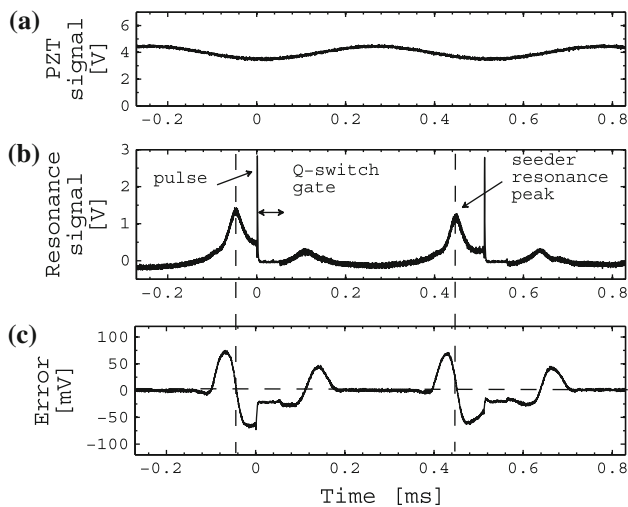


Fig. 2 **a** PZT sinusoidal modulation of the cavity length, **b** resonance of the DFB seeder injected inside the cavity. PRF of the 2- μm Q-switched pulsed oscillator is 2 kHz. **c** PDH error signal after demodulation. Seeder frequency external phase modulation is 90 MHz

polarization drifts that may cause undesirable amplitude fluctuations in the seeding or in the coherent detection for characterization.

The Online DFB is locked to the 2,050.967 nm CO_2 absorption line center using the PDH technique (Fig. 1) and a similar locking set-up as described in Numata et al. [26]. We developed an offset locking technique to tune the Offline DFB from 0.5 to 6 GHz away from the Online DFB wavelength. In this paper, an Offline offset of 3 GHz was chosen to demonstrate the two-wavelength seeding method of the same oscillator. Fine adjustment of the offset is achieved to ensure that On and Off DFB wavelengths are separated by an integer number of resonator free spectral ranges (FSR). This is done to avoid a too long excursion of the PZT for multiple wavelengths seeding. As initial phase, On and Offline DFB resonance peaks are superposed in time when the cavity length is modulated. The cavity length is then sequentially locked to the DFB resonance using a modified PDH technique [27, 28]. The DFBs are externally phase-modulated at 90 MHz using an electro-optic modulator (EOM) from Photline Technologies (model MPX2000-LN-0.1). That modulation produces two radiofrequency sidebands in opposite phase at ± 90 MHz around the optical carrier frequency. The seeder is then injected inside the cavity through the first AOM diffraction order at Bragg angle. A detector monitors the resonance signal from the leakage beam diffracted by the AOM. At a resonant position, both sidebands (which are in opposite phase) are equally transmitted and no beat notes are detected. Outside the resonance position, a beat note at 90 MHz appears on the detector used to monitor the

resonance. A signal demodulation allows the retrieval of an error signal that is processed by a proportional integral servo-controller (New Focus LB-1005) to adjust the PZT position back to the resonance position. Resonance and error signals examples are shown in Fig. 2.

The PZT is driven by a sinusoidal signal (Fig. 2a) to scan the ring cavity resonances. A detector shows the resonance peaks (Fig. 2b). The spikes in Fig. 2b are for the Q-switched laser pulse leaks from the AOM. The resonance peaks become larger as the crystal gain increases with time. The error signal (Fig. 2c) enables the locking of the cavity length to the resonance of the seeder. The servo-controller integration is stopped during each pulse emission to prevent perturbations of the feedback loop. Figure 2b shows that the resonance peak line widths are rather large (40 MHz FWHM) in comparison with the FSR of the cavity (300 MHz). This is mainly due to the low finesse of the resonator (large output coupler transmission). Several milliwatts are then necessary to get a sufficient signal to noise ratio on the PDH error signals to increase the precision of the locking system.

3 Experimental results

3.1 Free-running operation

Free-running operation of Ho:YLF and Ho:LLF oscillator in Q-switched regime have been widely documented in Schellhorn paper [15]. However, the 2- μm pulsed oscillator has not been designed and optimized for a DIAL emitter. We present here the results of such an optimization and the performances of a 80-mm-long 0.5 %-doped Ho:YLF crystal-based Q-switched π -linear polarized oscillator working at 2,051 nm. The output coupler was fixed at 50 % of reflectivity at 2,051 nm. Lower reflectivity is still possible to get a gain bandwidth centered at 2,051 nm but results in a higher threshold and a lower efficiency of the oscillator as reported by Schellhorn [15].

Given that such a DIAL emitter is expected to be associated both with lidar direct and coherent detection, we analyze its Q-switched performances as a function of the PRF. Figure 3 shows the pulse energy and pulse duration for a 37-W pump power and different PRF from 100 Hz to 10 kHz. From 100 Hz to 2 kHz, the average output power increases from 3.8 to 8 W but pulse energy decreases from 37 to 4 mJ. At high pulse repetition rate (above 2 kHz), the average output power remains constant around 8.5 W. FWHM pulse duration stays below 60 ns up to 1 kHz and then rises up to 270 ns at 10 kHz. The optical efficiency of the oscillator at 37 W pump power remains above 20 % up to 1 kHz and then decreases to 10 % at 100 Hz. The pump power was chosen to be limited to 37 W so that the

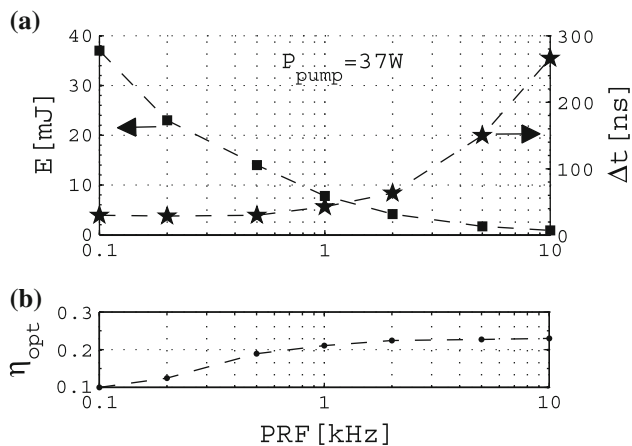


Fig. 3 Fixed pump power (37 W) and variable PRF operation. **a** Laser pulse energy (E) (squares and left axis) and laser FWHM pulse duration (Δt) (star and right axis). **b** Optical to optical efficiency (η_{opt})

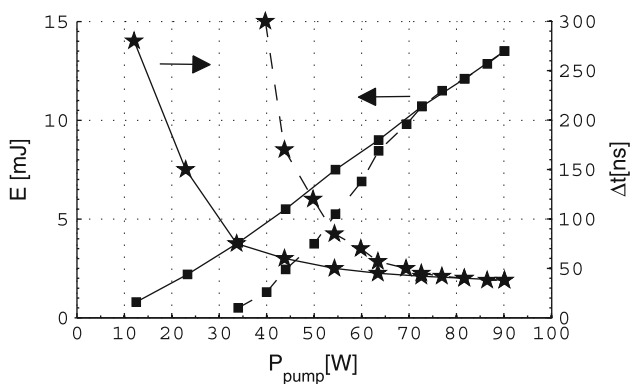


Fig. 4 Fixed PRF (2 kHz) and variable pump power operation. Pulse energy (E) (squares and right axis) and FWHM pulse duration (Δt) (stars and left axis). The dashed curves show the modification of slope efficiency when the pump beam focus is optimized at full pump power only

maximum intra-cavity fluence at 100 Hz is 28 J/cm^2 that is just below the announced damage threshold of the coatings of the crystal ($<30 \text{ J/cm}^2$). However, such an operation proved to be too closed to some optical coatings inside the cavity that were damaged during the experiment. Therefore, a MOPA configuration [29] is preferable to limit the intra-cavity fluence to few J/cm^2 .

Using our rate equation model and following the works by Innocenzi et al. [30] and Hardman et al. [31], we estimated the thermal focal lens inside the laser crystal at full pump power and found -2 m . The beam size in the crystal is then expected to change resulting in a modification of pump and oscillator mode overlap. Figure 4 shows pulse energy as a function of pump power at 2 kHz. The pump beam focus is experimentally adjusted for each data point to correct the crystal thermal lens. At 92 W pump power, we get 13.5 mJ pulse energy at 2 kHz resulting in a 30 %

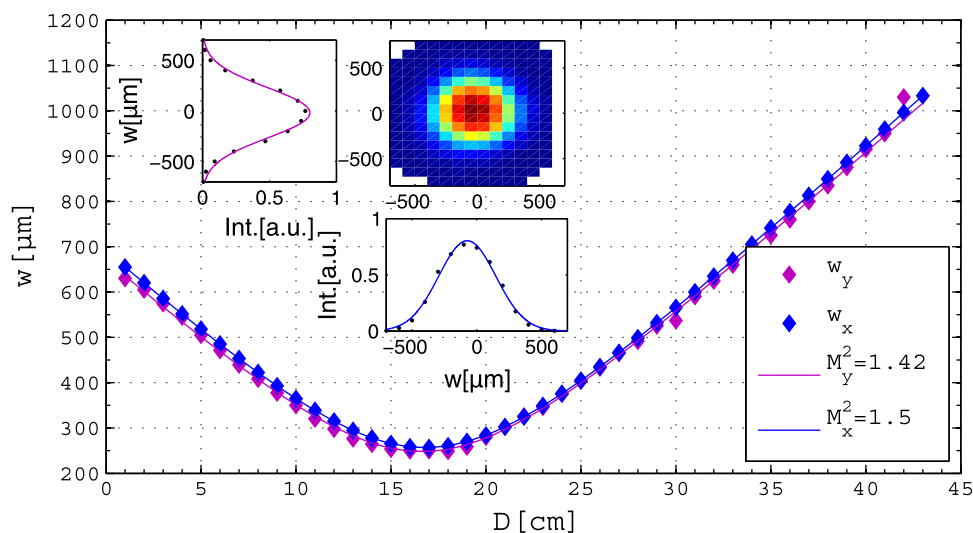
of optical efficiency at 2,051 nm. Given the EOE of our Tm-fiber laser (5 %), the electrical efficiency of the oscillator is 1.5 %. The electrical power required for cooling the fiber laser and the laser system (laser crystal and MAO) is not included in this calculation. The EOE could be increased by a factor of 4 (6 %) with current commercial Tm-fiber laser from ITF Labs. Figure 4 also shows that the pulse duration decreases as the pump power increases. At 92 W pump power, the pulse duration is reduced to 42 ns. The dashed curves show the modification of slope efficiency when the pump beam focus is optimized at full pump power only. The oscillator threshold increases from 14 to 37 W.

The spatial characteristics of the pulsed laser beam at full pump power were investigated using a Pyrocam III camera from Spiricon: beam profiles and widths, beam divergence and propagation factors (M^2). Figure 5 shows the evolution of the focused laser beam after it has been passed through a 45° total reflective dielectric mirror and a positive 250 mm focal length lens which was positioned approximately 400 mm from the output coupler. The insets show the horizontal and vertical beam profiles in the focus. All along the propagation, the fits to a Gaussian intensity distribution gave R^2 values larger than 0.99 in both directions. The beam widths were computed using the second moment width method ($D4\sigma$). The beam quality factors were determined by fitting the data by the standard Gaussian beam propagation expression. The measured $M_x^2 = 1.50$ and $M_y^2 = 1.42$ shows a slight deterioration of a pure Gaussian beam probably due to the effect of the thermal lens in the crystal.

3.2 Single-frequency injection-seeded operation

First single-frequency injection-seeding operation of a Ho:YLF oscillator was already mentioned at low PRF (100 Hz) in Botha et al. [19] at 2,064 nm but not fully characterized. Here, the seeding of the Ho:YLF oscillator is tested at high PRF (2 kHz) and the DFB seeder is locked to R30 CO_2 line center at 2,050.97 nm. For a DIAL emitter, the characterization of pulse energy and frequency stability of the seeding is fundamental to predict instrumental error on future gaseous concentration measurements. To do this, a slight part of the laser pulses is injected into a PM monomode fiber and is optically mixed with the 50-MHz acousto-optic frequency shifted (AOFS) part of the DFBs (Fig. 1). As the seeder is injected into the cavity through the first AOM diffraction order, the seeded wavelength is actually frequency shifted by 27.12 MHz. The resulting heterodyne beat note is detected at $\sim 78 \text{ MHz}$ (due to the additional 50 MHz frequency shift of the AOFS) with a balanced photoreceiver (Discovery Semiconductor Inc, DSC-R205 M). Two thousand and forty-eight samples are

Fig. 5 Spatial characteristics of the pulsed laser beam at full pump power. *Horizontal and vertical* beam half widths after an $f = 250$ mm lens. The beam widths are computed using the second moment width method ($D4\sigma$). Beam propagation factors (M^2) are indicated. The beam intensity profiles and adjusted Gaussian fit are shown in the insets



digitized at a 400 MSPS sampling rate. A spectrum is computed from each acquisition using a fast Fourier transform (FFT) algorithm. Figure 6 shows a typical pulse shape and the FFT of the heterodyne signal measured at 73 W pump level and at a PRF of 2 kHz. A high spectral purity can be seen with no other harmonic components within 25 dB of the main peak (thin lines are only due to parasitic signals from the AOFS). The FFT of the heterodyning signal is the convolution between the pulsed oscillator and the DFB seeder spectra. Given the 2.1 MHz linewidth of the DFB and using the inset of Fig. 6b, we estimate a pulsed oscillator linewidth of 8.2 MHz. It is nearly transform limited with the simultaneously recorded pulse duration of 55 ns (Fig. 6a). At full pump power, the laser pulse duration and spectral width become 42 ns and 11 MHz, respectively. To estimate the injection-seeding efficiency, statistics of both pulse energy and beat notes frequencies between the seeder and the laser pulses are computed. The beat note frequency is estimated using heterodyne detection and taking the maximum of each spectrum peak. The FFT spectrum frequency resolution is 100 kHz. The pulse energy is measured using a photodiode and estimated using direct measurement of the area of the pulse shape. One lakh and sixty thousand shots were sampled and processed to plot pulse energy and beat note frequency histograms (Fig. 7a, c). The two distributions have a Gaussian-like shape. Pulse energy relative standard deviation is 4.7 %. Frequency standard deviation is 2.6 MHz. Ninety-seven percentage of the beat note frequencies lie within \pm three times the standard deviation. We can notice that the mean frequency (81 MHz) differs from the expected 77 MHz frequency shift. The PDH error signal should be strictly an odd function; nevertheless, its shape is very sensitive to the alignment of the resonance detector. Discrepancy from a perfect odd function leads to

an offset in the locking point and could explain the difference between the mean beat note frequency and the seeder frequency shift. The beat note distribution only gives some information about the seeding process whatever the seeder frequency stability is. As DIAL measurements usually require pulse averaging, Allan deviation is a more relevant parameter to consider, regarding the laser pulse energy and frequency stabilities. Indeed, Allan deviation is convergent for most types of noises, whereas the standard deviation is only convergent for white noise [32]. The Allan variance for pulse frequency is defined by the following expression:

$$\sigma_v^2(\tau) = \frac{1}{m} \sum_{i=1}^m (v_{i+1} - v_i)^2 / 2 \quad (1)$$

where v_i is the i th of m frequency values averaged over the measurement interval τ . A similar expression of (1), where v_i is replaced by E_i , can be defined for Allan variance of pulse energy.

Figure 7b, d shows the pulse energy and beat note frequency Allan deviations as a function of the averaging time τ . We can notice that the Allan deviation at τ 0.5 ms equals the standard deviation. Concerning pulse frequency stability, for averaging times < 0.1 s, white noise is predominant and experimental data fit well with a white noise behavior ($\tau^{-1/2}$). Because of others types of noise processes, averaging times > 0.1 s hardly allows a better estimation of the beat note frequency. For 10 s time averaging, the Allan deviation is about 100 kHz. This successfully corresponds to space IPDA measurement requirements [6, 22]. For pulse energy stability, averaging times < 0.1 s enables a slight reduction in the standard deviation but less than the square root law. Between 0.1 and 10 s, low frequency noise expected from thermal and vibration variations on the optical bench may explain the curves flat

Fig. 6 **a** Laser pulse profile. The laser is injection-seeded and works at 73 W pump power and a PRF of 2 kHz. The pulse profile is fitted by a Gaussian function to determine the laser pulse duration of 55 ns. **b** Associated heterodyne beat note spectrum. The *inset* provides a zoom of the spectrum to calculate the spectral linewidth

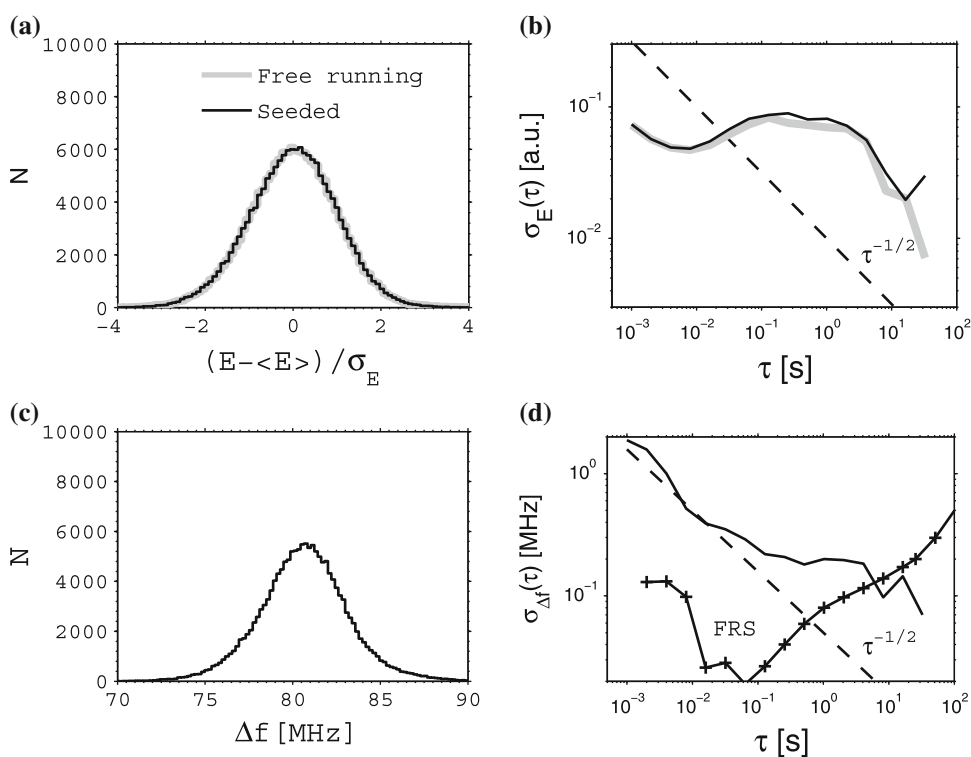
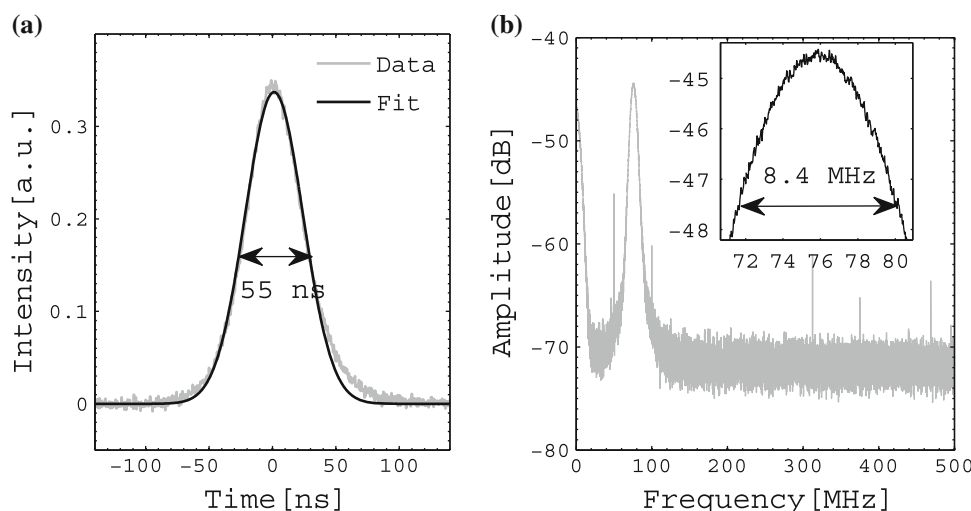


Fig. 7 Free-running and one-wavelength injection-seeded operations. **a** Normalized pulse energy distribution for free-running (*gray thick solid line*) and seeded (*black solid line*) operations. Relative standard deviation $\sigma_E/\langle E \rangle$ is 0.047 for seeded and 0.048 for free-running operation. **b** Allan plot for pulse energy. Pulse energy standard deviation is displayed in free-running (*gray thick solid line*) and seeded (*black solid line*) as a function of the sampling time. **c** Beat note frequency distribution for injection-seeding operation. Standard

deviation is $\sigma_{\Delta f} = 2.58$ MHz. **d** Allan plot for pulse frequency. Beat note frequency standard deviation is displayed as a function of the sampling time (*black solid line*). Line and marker (*crosses*) is for the Online DFB frequency standard deviation with respect to the R30 CO₂ absorption line center (FRS Allan plot). The dashed lines in panels **b**, **d** are for the expected decrease in standard deviation when only white noise is considered. N is the number of samples

behavior in Allan plot. For $\tau < 1$ s, Allan variance of the beat note is far larger than the Allan variance due to the FRS (line and marker curve in Fig. 7d). This is not the case anymore when τ increases and when thermal effects prevail in the noise fluctuations.

3.3 Two-wavelength injection-seeded operation

In the frame of DIAL measurements, two-wavelength injection-seeding operation is necessary which requires a sufficient gain bandwidth of the pulsed oscillator. When the

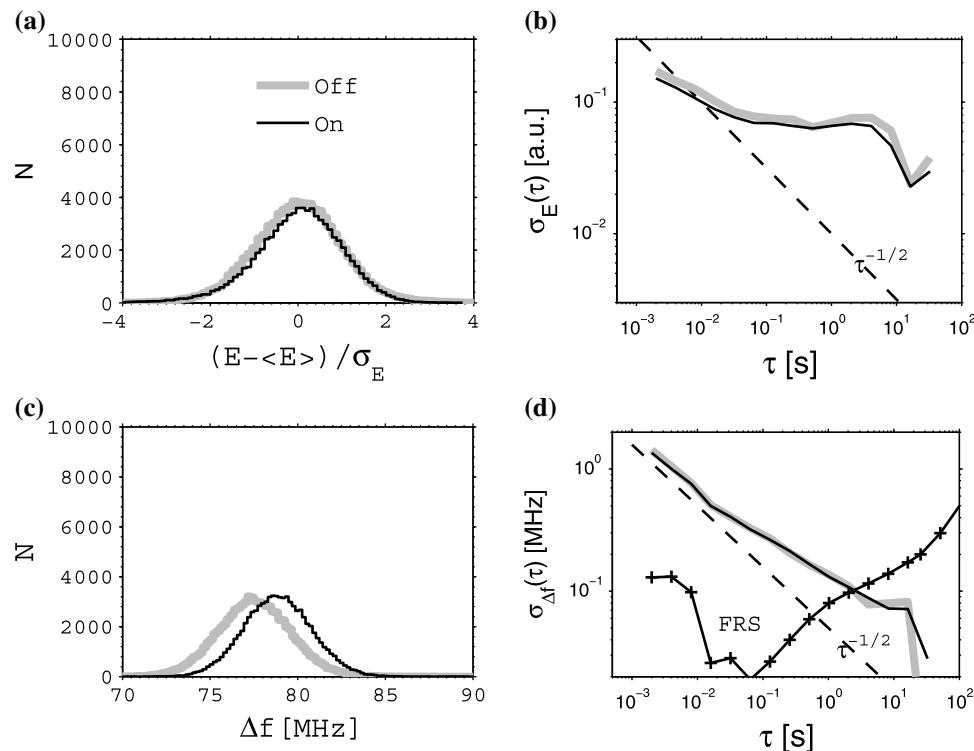


Fig. 8 Two wavelengths On and Offlines injection-seeded operation. **a** Normalized pulse energy distribution for Offline (gray thick solid line) and Online (black solid line) seeded wavelengths. Relative standard deviation are $\sigma_{E-Off}/\langle E_{Off} \rangle = 0.078$ and $\sigma_{E-On}/\langle E_{On} \rangle = 0.077$. **b** Allan plot for pulse energy. Online (black solid line) and Offline (thick gray solid line) pulse energy standard deviations are displayed as a function of the sampling time. **c** Online (black solid line) and Offline (gray thick solid line) beat note

frequency distribution for injection-seeding operation. Standard deviation are $\sigma_{\Delta f-Off} = 2.08$ and $\sigma_{\Delta f-On} = 1.94$ MHz, **d** Allan plot for frequency. Online (black solid line) and Offline (gray thick solid line) standard deviations for the beat note frequency are displayed as a function of the sampling time. As for Fig. 7, Allan plot for the FRS is also indicated and the dashed lines are for the expected decrease in standard deviation when only white noise is considered. N is the number of samples

Ho:YLF crystal is thermalized at 15 °C, the oscillator gain was measured to vary by <10 % between 2,050.5 and 2,052.2 nm. This was done looking at the seeder resonance peak amplitude from 2,049 to 2,053 nm (using DFB frequency tunability). This potentially enables the seeding of several wavelengths for CO₂ and H₂O DIAL measurements in this spectral domain [21]. However, several injection-seeded wavelengths and associated multiple servos pose an additional challenge for pulse energy and frequency stability of the same Ho:YLF pulsed oscillator. Between the two laser pulses, the ring cavity length has indeed to be finely adjusted to be resonant for the On and the Off wavelengths. The On wavelength is locked to the center of the R30 CO₂ line (2,050.97 nm) while the Off wavelength is locked at an integer number of oscillator FSR from the On wavelength and at approximately 3 GHz out of CO₂ absorption line center. Eighty thousand On and Off pulse pairs were sampled at 400 MHz. The same pulse energy and frequency stability calculations as for the one-wavelength seeding were made. Figure 8a, b characterizes the pulse energy stability at On and Off wavelengths. Similar pulse energy relative standard deviations are obtained for

both wavelengths (Off: 7.8 % and On: 7.7 %). However, the standard deviation is almost double than the single-wavelength seeding one. The Allan plot for pulse energy shows that this is the result of an increase in the noise at high frequency ($\tau < 0.1$ s). This additional noise is likely due to imperfect resonance locking of both wavelengths (slight differences in the odd functions and the locking points as mentioned before). This is confirmed by the different mean On (78.9 MHz) and Off (77.5 MHz) beat notes estimated from the frequency distributions displayed in Fig. 8c. No quantitative difference is seen in the frequency Allan deviation between On and Off wavelengths or between single-frequency and dual-frequency seeding operations. The Allan plot also shows a similar decrease in frequency standard deviation with time averaging for both wavelengths and with single-frequency seeding operation.

In addition to the work reported here, other seeding configurations have been tested. DFBs with a broader linewidths of 10 MHz have been successfully used as seeder with similar results concerning frequency stability and Allan variance calculations. The main drawback for such a seeder is the lower signal to noise ratio in case a

coherent detection is used for the characterization of the emitter. Concerning the robustness of the servos, we tested different external modulation at 25 or 40 MHz using commercial module from Toptica Photonics (PDD/F40), but we found that a frequency external modulation at 90 MHz was preferable to improve the pulse energy and frequency long-term stability of the oscillator once used as a DIAL emitter.

In the framework of DIAL measurements, the FRS should be locked to the center of the CO₂ absorption line and several wavelengths should be shifted out of it to match an optimal optical depth around 1 [24]. For CO₂ IPDA measurements from space, Online will be locked at 3 GHz away the R30 CO₂ absorption line center and Off-line at approximately 19 GHz away in the nearest absorption-free window [22].

4 Conclusion

A two-wavelength single-frequency ME–HR laser oscillator with Ho:YLF as active medium for DIAL application was demonstrated. The oscillator consists of a fiber-coupled, free-space solid-state hybrid system. It sequentially produces On and Off single-frequency laser pulses with 13.5 mJ of energy at a repetition rate of 2 kHz and pulse duration of 42 ns. The spectral width of the laser pulses, 11 MHz, is nearly transform limited and is suitable for DIAL measurements of CO₂ or H₂O in the 2,050 nm domain. For the experiment reported here, the On wavelength was locked to the R30 CO₂ absorption line at 2,050.97 nm while the Off wavelength was offset locked 3 GHz apart to test the multiple wavelength seeding of the oscillator. HE–MR configuration (37 mJ at 100 Hz) worked as well as ME–HR one but we faced optical coating damage issues that could be solved using a MOPA configuration. Optical to optical efficiency of the oscillator is 30 % at 2 kHz and is reduced to 10 % at 100 Hz that leads to electrical to optical efficiencies between 6 and 2 % with commercially available Tm-fiber laser from ITF labs. The beam quality ($M^2 \sim 1.4$) shows a slight deterioration of a pure Gaussian beam probably due to the effect of the thermal lens in the crystal. Pulse energy and frequency stability have been widely studied in this paper using a coherent detection for characterization. Standard deviation is 7.7 % for pulse energy and 2 MHz for frequency stability for the two-wavelength seeding operation. Allan variance plot shows that frequency fluctuations are reduced below 70 kHz for 10 s of averaging which is suitable for accurate CO₂ DIAL or IPDA measurements. The stability of the system could be further improved using a better signal to noise in the optical and electronic seeding chain. In addition, the Allan variance plots show that pulse energy

and frequency fluctuations do not fit well with a white noise behavior suggesting that other type of disturbances have to be taken into account like vibrations, acoustic wave and thermal fluctuations.

Acknowledgments This work has been achieved in the framework of CO₂ and Wind Lidar (COWI) development supported by the French National Agency (project SENTINELLE: ANR-07-PCO2-007), the French National Space Agency (CNES) and the French National Research Center (CNRS) through the Institut National des Sciences de l'Univers (INSU-CNRS). The authors would also like to thank the French aerospace lab (ONERA), especially Guillaume Canat and Erik Lucas who build the 2- μ m TDFA and also LMD mechanical engineers, Olivier Godde and Olivier Bousquet for their contributions to the project.

Open Access This article is distributed under the terms of the Creative Commons Attribution License which permits any use, distribution, and reproduction in any medium, provided the original author(s) and the source are credited.

References

1. F. Gibert, P.H. Flamant, D. Bruneau, C. Loth, *Appl. Opt.* **45**, 4448 (2006)
2. G.J. Koch, J.Y. Beyon, B. Barnes, M. Petros, J. Yu, F. Amzajerdian, M. Kavaya, U.N. Singh, *Opt. Eng.* **46**, 116201 (2007)
3. G.J. Koch, J.Y. Beyon, F. Gibert, B.W. Barnes, S. Ismael, M. Petros, P.J. Petzar, J. Yu, E.A. Modlin, K.J. Davis, U. Singh, *Appl. Opt.* **47**, 944 (2008)
4. S. Ishii, K. Mizutani, H. Fukuoka, T. Ishikawa, B. Philippe, H. Iwai, T. Aoki, T. Itabe, A. Sato, K. Asai, *Appl. Opt.* **49**, 1809 (2010)
5. G. Ehret, C. Kiemle, M. Wirth, A. Amediek, A. Fix, S. Houweling, *Appl. Phys. B* **90**, 593 (2008)
6. P.H. Flamant, F. Gibert, D. Edouart, J. Cuesta, F. Marnas, D. Bruneau, ASCOPE MAG, in *Proceedings of the 24th International Laser Radar Conference (ILRC)*, paper No S110-11, 1118, (2008)
7. D.P. Schrag, *Science* **315**, 812 (2007)
8. F. Gibert, D. Edouart, C. Cenac, F. Le Mounier, O. Godde, O. Bousquet, P.H. Flamant, P. de Donato, Sentinelle project team, in *Proceedings of the 26th International Laser Radar Conference (ILRC)*, paper No S70-06, 843, (2012)
9. J.C. Baudron, P. Allard, J.P. Toutain, *Nature* **344**, 51 (1990)
10. F. Gibert, G.J. Koch, J.Y. Beyon, T.W. Hilton, K.J. Davis, A. Andrews, P.H. Flamant, U.N. Singh, *J. Atmos. Oceanic Technol.* **28**, 365 (2011)
11. T. Fan, G. Huber, R.L. Byer, P. Mitzscherlich, *IEEE J. Quantum Electron.* **24**, 924 (1988)
12. M. Schellhorn, A. Hirth, C. Kieleck, *Opt. Lett.* **28**, 1933 (2003)
13. M. Schellhorn, *Appl. Phys. B* **91**, 71 (2008)
14. S. Lamrini, P. Koopmann, M. Schäfer, K. Scholle, P. Fuhrberg, *Appl. Phys. B* **106**, 315 (2012)
15. M. Schellhorn, *Appl. Phys. B* **103**, 777 (2011)
16. P.F. Moulton, G.A. Rines, E.V. Slobodtchikov, K.F. Wall, G. Frith, B. Samson, A.L.G. Carter, *IEEE J. Sel. Top. Quantum Electron.* **15**(1), 85 (2009)
17. M. Haverkamp, K. Wieching, M. Traub, K. Boucke, *Proc. SPIE* **6456**, 64560U (2007). doi:10.1117/12.701869
18. C. Bollig, M.J.D. Esser, C. Jacobs, W. Koen, D. Preussler, K. Nyangaza, M. Schellhorn, Conference on middle-infrared coherent sources, (Eur. Phys. Soc.) Invited Talk Mo3. (2009)

19. L.R. Botha, C. Bollig, M.J.D. Esser, R.N. Campbell, C. Jacobs, D.R. Preussler, *Opt. Express* **17**, 20615–20622 (2009)
20. E.D. Black, *Am. J. Phys.* **69**, 79 (2001)
21. L. Joly, F. Marnas, F. Gibert, D. Bruneau, B. Grouiez, P.H. Flamant, G. Durry, N. Dumelie, B. Parvitte, V. Zéninari, *Appl. Opt.* **48**, 5475 (2009)
22. J. Caron, Y. Durand, *Appl. Opt.* **48**, 5413 (2009)
23. N.P. Barnes, B.M. Walsh, E.D. Filer, *J. Opt. Soc. Am. B* **20**(6), 1212 (2003)
24. D. Bruneau, F. Gibert, P.H. Flamant, J. Pelon, *Appl. Opt.* **45**, 4898 (2006)
25. Y. Pawela, N. Grossard, F. Le Mounier, F. Gibert, J. Hauden, *IEEE Photon. Technol. Lett.* **23**, 1163 (2011)
26. K. Numata, J.R. Chen, S.T. Wu, J.B. Abshire, M.A. Krainak, *Appl. Opt.* **50**, 1047 (2011)
27. V. Wulfmeyer, M. Randall, A. Brewer, R.M. Hardesty, *Opt. Lett.* **25**, 1228 (2000)
28. M. Ostermeyer, T. Waltinger, M. Gregor, *Opt. Commun.* **282**, 3302 (2009)
29. M. Schellhorn, M. Eichhorn, *Appl. Phys. B* **109**, 351 (2012)
30. M.E. Innocenzi, H.T. Yura, C.L. Fincher, R.A. Fields, *Appl. Phys. Lett.* **56**, 1831 (1990)
31. P.J. Hardman, W.A. Clarkson, G.J. Friel, M. Pollnau, D.C. Hanna, *IEEE J. Quantum Electron.* **35**(4), 647 (1999)
32. D.W. Allan, *Proc. IEEE* **54**(2), 221 (1966)